Article

Rolling Adhesion of Schizont Stage Malaria-Infected Red Blood Cells in Shear Flow

Anil K. Dasanna,[1,2] Christine Lansche,[3] Michael Lanzer,[3] and Ulrich S. Schwarz[1,2,*]

[1]BioQuant-Center for Quantitative Biology, [2]Institute of Theoretical Physics, and [3]Department of Infectious Diseases, Heidelberg University, Heidelberg, Germany

ABSTRACT   To avoid clearance by the spleen, red blood cells infected with the human malaria parasite *Plasmodium falciparum* (iRBCs) adhere to the vascular endothelium through adhesive protrusions called "knobs" that the parasite induces on the surface of the host cell. However, the detailed relation between the developing knob structure and the resulting movement in shear flow is not known. Using flow chamber experiments on endothelial monolayers and tracking of the parasite inside the infected host cell, we find that trophozoites (intermediate-stage iRBCs) tend to flip due to their biconcave shape, whereas schizonts (late-stage iRBCs) tend to roll due to their almost spherical shape. We then use adhesive dynamics simulations for spherical cells to predict the effects of knob density and receptor multiplicity per knob on rolling adhesion of schizonts. We find that rolling adhesion requires a homogeneous coverage of the cell surface by knobs and that rolling adhesion becomes more stable and slower for higher knob density. Our experimental data suggest that schizonts are at the border between transient and stable rolling adhesion. They also allow us to establish an estimate for the molecular parameters for schizont adhesion to the vascular endothelium and to predict bond dynamics in the contact region.

INTRODUCTION

Tropical malaria is a debilitating, life-threatening infectious disease caused by the eukaryotic parasite *Plasmodium falciparum* (1). Clinical manifestation and pathology of falciparum malaria are largely attributed to the asexual development of the parasite inside infected red blood cells (iRBCs) (2). Development of the malaria parasite within an iRBC takes ~48 h and can be divided into three morphologically distinct stages (3,4). During the first-half of the cycle, the parasite mainly rearranges itself into a ring shape inside the iRBCs. During the trophozoite stage (24–36 h postinvasion), the growing parasite remodels its host cell. In particular, it mines actin monomers from the spectrin network of the RBC to further develop the protein export system from the parasite to the cell surface (5–7). In the final schizont stage (40–48 h postinvasion), the iRBC becomes spherical, mainly due to changes in osmotic pressure (8–11). At the same time, the spectrin network is increasingly corrupted and the iRBC bursts open after 48 h (12,13).

To increase residency time in the vasculature and to avoid clearance by the spleen, an iRBC becomes adhesive and starts to stick to the microvascular endothelium, leading to impaired tissue perfusion, hypoxia, and systemic microvascularitis (2). In detail, during the late ring stage, at ~16 h postinvasion, the iRBC starts to develop adhesive protrusions on its surface, termed "knobs". These knobs can be visualized with electron microscopy (14–16) and atomic force microscopy (17,18). Early measurements reported that their density increases from ~20 to $60/\mu m^2$ from trophozoite to schizont (15), but these numbers are very variable and differ considerably between different malaria strains. For the strain used here, the knob density increases from ~9 to $15/\mu m^2$ from trophozoite to schizont (19). With a RBC surface area of $A = 136\ \mu m^2$ that is approximately constant over the developmental cycle (11), this corresponds to an increase of the numbers of knobs from $N_k \approx 1000$–2000. Interestingly, whereas the height of the knobs seems to be relatively constant, their diameter decreases with time.

Cytoadherence of iRBCs is mediated by several adhesion molecules produced by the parasite and localized to the knobs (in the following called "receptors"). The most prominent one is *P. falciparum* Erythrocyte Membrane Protein-1 (PfEMP-1), a family of immunovariant adhesins that can confer adhesive interactions with a broad range of host molecules (in the following called "ligands"), including CD36, ICAM-1, ECPR, and CSA. The ability of PfEMP-1 receptors to bind to different host ligands leads to organ-specific pathology, such as cerebral malaria or placental malaria (1).

CrossMark

The main host ligand that leads to firm adhesion to microvascular endothelium cells is CD36, whereas rolling is believed to be mediated mainly by ICAM-1 (20–24).

Formation of knobs also alters the spectrin network underlying the plasma membrane. It was shown by atomic force microscopy that the spectrin network is denser and sparser in knobby and nonknobby regions, respectively, and that the spectrin length increases during the replicative cycle (25). Using multiscale modeling, it has been argued that the vertical linking between the knobs and the spectrin network strongly changes the mechanics of the host cell (26). The number of PfEMP-1 receptors per knob (in the following called "receptor multiplicity") is not known, but has been estimated from flow chamber experiments to be approximately seven molecules (27). The fact that the knob size decreases during development suggests that receptor multiplicity might change over time.

Whereas uninfected RBCs have their typical biconcave shape, iRBCs become increasingly spherical as they move through the infection cycle. They attain an almost spherical shape at the schizont stage (10,11). The osmotic-colloidal model posits that these shape changes are related to the induction of new permeation pathways in the membrane and the influx of cations and accompanying water, leading to a higher osmotic pressure inside the cell (8,9) and a volume increase of 60% (11). In addition, the stiffness of the iRBC increases by up to one order of magnitude during the 48 h cycle, as shown by flow chamber and optical tweezer experiments (28–30) and explained by multiscale modeling (31–33). This increased stiffness will also contribute to a rounder shape.

Adhesion under flow conditions does not only occur for iRBCs, but also for white blood cells (WBCs) trafficking with the blood stream. In particular, rolling adhesion of WBCs can be seen in vivo as the first step toward extravasation during an acute inflammation (34,35). WBC rolling has been studied in vitro by flow chamber experiments, where cell rolling is monitored on ligand-coated substrates or endothelial monolayers. In contrast to the iRBCs, WBCs use receptors from the selectin-family for capture and rolling, and these are localized to hundreds of microvilli rather than thousands of knobs. Yet the basic design principle (elevated platforms for adhesion receptors distributed over a roundish cell shape) is very similar and therefore iRBC-rolling can be considered as mimicry of WBC-rolling (36). In particular, flow chamber experiments are also commonly used to study rolling adhesion of iRBCs (19,23,27,37).

Rolling adhesion of spherical WBCs can be modeled with adhesive dynamics as pioneered by Hammer and Apte (38) and Hammer (39), who predicted which dynamic states (firm adhesion, rolling adhesion, free flow) should result from the underlying molecular properties. This approach has also been used to study two-receptor system (40) and catch-slip bond behavior (41). To make better contact to the molecular properties of the adhesion receptors, this model has been extended to spatially resolved receptor and ligand positions (42,43), again leading to the identification of dynamic states in state diagrams (44). During recent years, different aspects of rolling adhesion have been studied with this approach in more detail, including the role of microvilli extension (45) and the role of fluctuations during rolling adhesion (46). Rolling adhesion has also been studied for deformable cells (47) and a state diagram has been simulated as a function of cell adhesion and deformability (48). This work has shown that a modest deformability stabilizes adhesion due to an increase in the contact area, but that strong deformability suppresses adhesion because thin shell mechanics leads to the contact area deforming away from the adhesive substrate.

In contrast to WBCs, uninfected RBCs are neither adhesive nor spherical. Their biconcave shape necessitates computationally expensive computer simulations. The three most prominent methods to simulate the movement of uninfected RBCs in hydrodynamic flow are the lattice Boltzmann method (49), multiparticle collision dynamics (50), and dissipative particle dynamics (51,52). The dissipative particle dynamics approach has also been combined with rules for adhesion to model cytoadherence of iRBCs (31,53,54). However, because it is computationally very demanding, it is difficult to obtain a comprehensive understanding of the relation between the molecular properties and the dynamic states with this approach.

Here we reason that such a comprehensive treatment should become possible in the schizont stage of iRBCs, for which shape is known to become close to round (10,11) and thus should allow the application of adhesive dynamics for round shapes (38,44). We therefore have conducted flow chamber experiments for iRBCs moving over endothelial monolayers, in which we track not only translational velocity, as commonly done for WBCs in flow chambers, but also make use of the presence of the parasite to track rotational velocity, which before has been done only for Janus particles (55) and leukemia cells with intracellular granular structures (56). Using this approach, we can demonstrate experimentally that cell movement in the trophozoite stage corresponds more to flipping than to rolling, as suggested before by computer simulations for deformable cells (31,53,54), and that smooth rolling emerges in the schizont stage. This then justifies our using adhesive dynamics for spherical cells to simulate the state diagrams that predict how the dynamic states of rolling cells should depend on knob density and multiplicity. We finally use our experimental results to provide an estimate for the molecular parameters of iRBCs in the schizont stage.

MATERIALS AND METHODS

Cell culture

Human dermal microvascular endothelial cells (HDMECs) were purchased from Promocell (Heidelberg, Germany) and grown in endothelial cell

growth medium MV (Promocell) without antibiotics or antimycotics, at 37°C in a humidified incubator with 5% CO_2. Subculturing was performed as recommended by the manufacturer. Cells were used for experiments between passages 6 and 7.

The *P. falciparum* FRC3 strain was cultured as described by Trager and Jensen (57). Briefly, parasites were cultured in type A^+ erythrocytes suspended in RMPI 1640 medium supplemented with 2 mM L glutamine, 25 mM HEPES, 100 μM hypoxanthine, 20 μg/mL gentamicin, and 10% human A^+ serum. Cells were grown at a hematocrit of 3.5% at 37°C under controlled atmospheric conditions (3% CO_2, 5% O_2, and 92% N_2). Parasites were tightly synchronized within a time window of 6 h using the sorbitol lysis method (58). The parasite stage was monitored by Giemsa-stained blood smears. To ensure a parasite population capable of cytoadhering to HDMECs, parasites were repeatedly selected for a knobby phenotype by gelatin flotation (59) and panned over HDMECs (60). Late stages were enriched using the magnetic cell sorting method (61) yielding a parasitemia of >95%. iRBCs were labeled with 0.4 μL/mL SYBR Green for 1 h at 37°C for automated cell tracking.

Flow chamber experiments

HDMECs were grown to confluency under static conditions on disposable flow chambers with parallel plate geometry (μ-slide VI0.4; Ibidi, Martinsried, Germany), and the flow chambers were coated with fibronectin (10 μg/mL in PBS). Microslides containing confluent HDMECs were washed twice with binding medium (RPMI 1640 supplemented with 2 mM L-glutamine, 25 mM HEPES, and 0.1% (v/v) BSA, pH 7.2, adjusted with NaOH) and mounted on the stage of an inverted microscope. One end of the microslide was connected to a high precision syringe pump (55–2316; Harvard Apparatus, Holliston, MA) via silicon tubing (Ibidi), permitting the perfusion of a cell suspension prewarmed to 37°C at a controlled flow rate, generating a desired continuous laminar shear stress.

For the flow assay, a suspension of 10^6 iRBCs/mL (in binding buffer at 37°C) was applied over the confluent cell monolayer in the microfluidic chamber at different shear stress values, ranging from 0.03 to 0.10 Pa. The shear stress for a given shear viscosity η and a given shear rate $\dot{\gamma}$ is $\tau = \eta\dot{\gamma}$. As the measured viscosity of the used medium is 0.7 mPa s, this corresponds to a range of shear rates used in our experiments as being from 42 to 142 Hz. For each shear stress condition, the SYBR Green fluorescence signals or the differential interference contrast images were recorded (time interval 0.033 s) in different fields along the center line of the chamber, where homogeneous flow is found, using an inverted microscope (40× magnification, EGFP HC Filter set Ex: 456–490 nm Em: 500–540 nm; Zeiss Axio Observer; Carl Zeiss, Oberkochen, Germany). Note that for the differential interference contrast images the contrast comes from the malaria pigment (hemozoin) rather than from the nucleus. Velocities and fluorescence intensity profiles were obtained after fluorescence video analysis using the TrackMate plugin from ImageJ (Version 2.7.3; National Institutes of Health, Bethesda, MD). Only cells that showed an end-to-end motion were used for analysis.

Stokesian dynamics

In Fig. 1 we show a schematic representation of the situation investigated here. We consider simple linear shear flow as used in flow chamber experiments, thus the unperturbed flow field reads $u^\infty = \dot{\gamma}z\mathbf{e}_x$. For a typical shear rate $\dot{\gamma} = 100$ Hz and a typical cell radius $R = 4$ μm, the typical flow velocity is $v = \dot{\gamma}R = 400$ μm/s. Therefore, the Reynolds number is $Re = \rho v R/\eta \approx 10^{-3}$ and we deal with overdamped dynamics and the Stokes equation for hydrodynamic flow. Thus we describe cell movement by an overdamped Langevin equation (42–44), as follows:

$$\partial_t X(t) = u^\infty + M\{F_D + F_S\} + k_B T\nabla M + \xi(t), \quad (1)$$

where $X(t)$ is a six-dimensional vector representing both position and orientation. Here the six-dimensional generalized forces F_D and F_S represent the
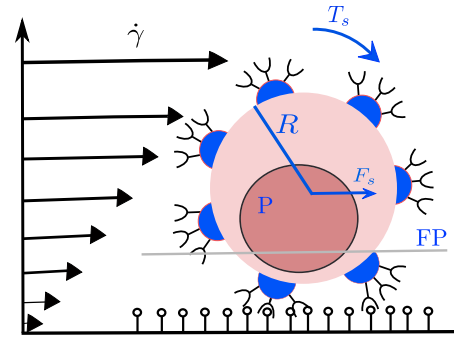

FIGURE 1 Schematic diagram of the computational model showing a spherical (schizont) iRBC of radius R rolling in shear flow with shear rate $\dot{\gamma}$. The spatially resolved receptors on the cell surface are localized to parasite-induced knobs and can form molecular bonds with the spatially resolved ligands on the substrates, which have a uniform density. The shear force F_s and the shear torque T_s lead to translational velocity v and rotational velocity Ω, depending on the details of the spatial receptor and ligand distributions and of the bond dynamics. The parasite P is labeled by fluorophores that are excited in the focal plane (FP). To see this figure in color, go online.

direct and shear-mediated forces and torques, respectively. The direct forces in turn include gravitational force and receptor-ligand bond forces. M is the 6×6-mobility matrix that has to be calculated from the Stokes equation for a sphere above a wall (43). The stochastic random force, $\xi(t)$, is multiplicative noise as the mobility matrix depends on the position of the sphere above the wall. The multiplicative nature of the noise leads to a spurious drift term ∇M.

To make Eq. 1 nondimensional, we scaled all the lengths by the radius R of the cell, time by inverse shear rate, $1/\dot{\gamma}$, and forces by the Stokes force at a typical velocity, $6\pi\eta R^2\dot{\gamma}$. We solve the discretized version of Eq. 1, which is given by the following:

$$X(\tau + \delta\tau) = X(\tau) + [u^\infty + M\{F_D + F_S\}]\delta\tau$$
$$+ \frac{1}{Pe}\nabla M|_\tau \delta\tau + \sqrt{\frac{1}{Pe}} B \times \xi(\tau), \quad (2)$$

with the dimensionless Peclet number, $Pe = (6\pi\eta R^3\dot{\gamma})/(k_B T)$ measuring the ratio between advection and diffusion. At low Peclet numbers, the motion is dominated by stochastic diffusion, whereas at high Peclet numbers, the motion is dominated by deterministic motion in the flow. B follows from $M = BB^T$ and we use Cholesky decomposition to determine B (62). In the last term, $\xi(t)$ is a six-dimensional random vector generated using the Gaussian distribution with mean = 0 and standard deviation = 1.

Bond dynamics

Receptors and ligands are placed on the cell and on the substrate, respectively, at fixed positions according to the desired spatial distribution. We employed stochastic bond dynamics between receptors and ligands during each time step. Because we have spatially resolved reaction patches, we use the concept of an encounter complex, meaning that receptor-ligand bonds can only be formed when the distance is less than the encounter distance r_0. A bond can then be formed between receptor and ligand with constant on-rate κ_{on}. The probability for the formation of the bond is $P_{on} = 1 - \exp(-\kappa_{on}\delta\tau)$. For bond dissociation, we use Bell's equation for slip bonds, $\kappa_{off} = \kappa_{off}^0\exp(F/F_d)$, where κ_{off}^0 is unstressed off-rate and F_d is the internal force scale (63). Although catch-slip bonds have been reported for leukocyte adhesion (64) and although there is evidence for shear-enhanced binding of iRBCs (19), in the absence of detailed

molecular information here we use a slip bond. The probability for bond dissociation is $P_{off} = 1 - \exp(-\kappa_{off}\delta\tau)$. We modeled the mechanics of the receptor-ligand bond as a cable, as follows:

$$F(r) = k(r - \ell_0)\Theta(r - \ell_0), \qquad (3)$$

where Θ is the Heaviside step function, k is the spring constant, and ℓ_0 is the bond length at the time of bond formation.

Receptor distribution

Cytoadherence of iRBCs results from the presence of knobs. To study the role of knob distribution in enhancement of adhesion, we modeled the knobs as a cluster of receptors on a spherical surface (Fig. 1). To achieve a variable degree of clustering of the receptors, we use a Monte Carlo simulation with a potential energy for their distribution (65,66). The total potential is as follows:

$$V(r_{i,j}) = \rho D\left(e^{-2(r_{i,j}-r_0)/\lambda} - 2e^{-(r_{i,j}-r_0)/\lambda}\right) \\ + Ae^{-r_{i,j}/m}/(r_{i,j}/m). \qquad (4)$$

The first term is the Morse potential, which acts as a short-ranged attractive potential. The second term is a Yukawa potential, which acts as long-range repulsive potential. The depth of Morse potential is given by D, and λ defines the width of potential well. We used $D = 1$ k_BT, $\lambda = 0.03$, and the equilibrium distance $r_0 = 150$ nm. For the Yukawa potential, the prefactor A is set to 0.01 k_BT and the decay length is $m = 2$. The dimensionless number $\rho \in [0,1]$ is used to modify the degree of clustering. When ρ is 0, the attractive potential vanishes, whereas when ρ is close to 1, the potential is dominated by attractive potential at short distances and repulsive potential at longer distances. The initial configuration is constructed by randomly distributing the receptors on the spherical surface, and then Metropolis dynamics at dimensionless temperature $T = 0.1$ is used to arrive at the final receptor configuration.

Classification of dynamic states

For given model parameters, which include the bond kinetic rates, the shear rate, and the spatial distribution of receptors and ligands, different dynamic states are possible, which in turn determine cellular function. To classify different dynamic states, we adopt a classification scheme based on the averages and variances of the translational and angular velocities (36,44). Each cell trajectory belongs to one of the five dynamic states, namely free motion, transient motion-1, transient motion-2, rolling adhesion, and firm adhesion. As the shear flow is applied only in the x direction, we only consider the x component of the translational velocity, $v_x(t)$, and the y component of the angular velocity, $\Omega_y(\tau)$. The other components are almost negligible unless one works with very low shear rates. During free motion, both translational and angular velocities have values almost equal to that of a free cell moving close to the wall, as there is a negligible number of bonds; thus, we define this state by $\langle v \rangle > 0.95\langle v^{hd}\rangle$, where the hydrodynamic reference value follows from a simulation without bond formation. Firm adhesion is defined by $\langle v \rangle < 0.01\langle v^{hd}\rangle$. For free motion, it is known from the solution of the Stokes equation that the cell is slipping over the substrate with $R\langle\Omega\rangle/\langle v\rangle \approx 0.56$ (44,67). During rolling adhesion, bonds continuously form and break, resulting in reduction in translational and angular velocities compared to free motion. Now translational and rotational velocities are synchronized such that $R\langle\Omega\rangle/\langle v\rangle \approx 1$. Therefore, we define rolling adhesion by $\langle v \rangle > 0.01\langle v^{hd}\rangle$ and $R\langle\Omega\rangle/\langle v\rangle > 0.8$. Transient adhesion is also characterized by an appreciable velocity, $\langle v \rangle > 0.01\langle v^{hd}\rangle$, but the coordination between translation and rotation is not as strong as in rolling adhesion, $R\langle\Omega\rangle/\langle v\rangle < 0.8$. Finally, transient adhesion-1 is less erratic than transient adhesion-2 ($\sigma_v/\langle v\rangle < 0.5$ and > 0.5, respectively). Whereas the cell is only

occasionally slowed down in the first case, in the second case it undergoes stop-and-go (or stick-slip) motion.

RESULTS

Differential adhesion behavior of trophozoites and schizonts under flow

To test under which conditions smooth rolling occurs, we investigated the rolling behavior of iRBCs on HDMECs under flow. Cytoadherence on HDMECs is mediated by CD36 and ICAM-1 (22–24), of which they have been measured to contain $86 \pm 14 \times 10^6$ and $6 \pm 3 \times 10^6$ molecules/mm², respectively (22). However, ICAM-1 is thought to be the primary ligand for rolling, whereas CD36 supports rolling adhesion only within a narrow velocity range and is mainly considered as ligand for firm adhesion (22,24,37). Wall-shear stresses in the range from 0.03 to 0.10 Pa (corresponding to shear rates from 42 to 142 Hz) were chosen to represent the range of physiological hydrodynamic conditions under which rolling adhesion iRBCs occurs in postcapillary venules and sinusoids (68–70).

We first compared the differential behavior of trophozoites versus schizonts, which were selected 24 ± 6 and 40 ± 6 h postinvasion, respectively. Fig. 2 A shows that the trophozoite is still biconcave and that the parasite sits at the periphery of the iRBC. In marked contrast, Fig. 2 B shows that the schizont is almost round and that now the parasite mass completely fills the middle of the cell. The three selected frames of representative rolling cells shown in Fig. 2, C and D (full movies provided as Movies S1 and S2) for trophozoites and schizonts, respectively, indicate that schizont rolling is much smoother, as expected from the shape and confirmed by the corresponding movies. One also sees that the schizont is larger than the trophozoite, and that the parasite location has shifted from the periphery to the middle of the iRBCs.

To obtain quantitative data on cell motion, we have labeled iRBCs with the fluorescent DNA-stain SYBR Green and followed the behavior of single cells, using automated imaging and tracking tools. For each cell two traces were obtained, the translational velocity and the fluorescence amplitude profile, as shown in Fig. 3 (primary data provided as Movies S3 and S4). For a smoothly rolling cell of spherical shape, the amplitude should be perfectly oscillatory, with the mathematical form of a curtate cycloid (see Fig. 1). When comparing the trophozoite data in Fig. 3 A with the schizont data in Fig. 3 B, one sees that the trophozoite shows strong changes in rolling velocity $v(t)$ and a very asymmetric amplitude trace. Although not completely symmetric, the fluorescence track of the schizont cell is much more symmetric and the rolling velocity $v(t)$ is much smoother. Most strikingly, there is a clear correlation between velocity and amplitude in the trophozoite case in Fig. 3 A (marked with *ellipses*): each time its velocity bursts,
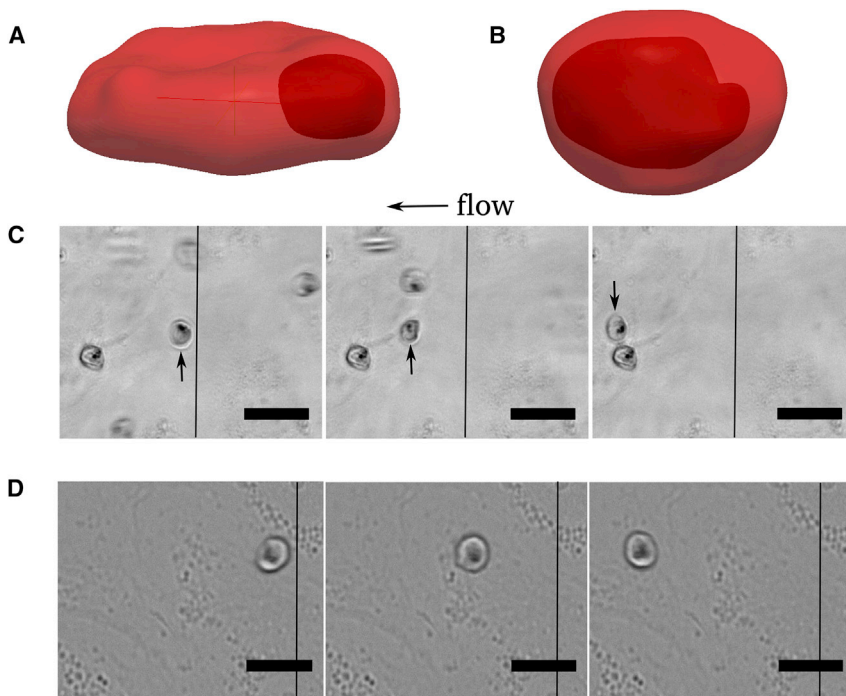
A **B**

← flow

C

D

FIGURE 2 Trophozoites and schizonts show very different behavior in shear flow. (*A*) In the trophozoite stage, the iRBC is still biconcave and the single parasite is situated at the rim. (*B*) In the schizont stage, the iRBC is almost spherical and the parasite mass almost fills the complete host cell (reconstructed from confocal microscopic images, as described elsewhere (11)). (*C*) Shown here are three frames of a trophozoite moving over an endothelial monolayer in shear flow from right to left (shear rate 142 Hz, cell marked with *arrows*; the other cells are firmly attached). The full sequence is provided as Movie S1. (*D*) Shown here are three frames of a schizont rolling over the monolayer with the shear flow from right to left (shear rate 42 Hz). The full sequence is provided as Movie S2. Scale bars = 20 μm. To see this figure in color, go online.

the amplitude goes down, indicating that the periphery of the cell with the fluorescently labeled parasite makes a large excursion away from the focal plane once the cell accelerates. This behavior is typical for flipping motion, as predicted before by computer simulations for adhesive iRBCs with biconcave shape (31–33).

We also measured the Pearson correlation coefficient for the two trajectories shown in Fig. 3. For the trajectory of the trophozoite, the Pearson correlation coefficient is −0.632, whereas for the schizont trajectory it is −0.01. This means that for the trophozoite, translational velocity and amplitude are strongly correlated, and that this correlation is much weaker for the schizont. These findings imply that flipping motion is much more prominent during the trophozoite stage than during the schizont stage. Schizonts are more round in shape (compare Fig. 2, *A* and *B*) and less deformable, which inhibits the flipping behavior. Another interesting item of information derived from the amplitude profile is that the fluctuation amplitude is higher for trophozoites than for schizonts (Fig. 3), reflecting the more symmetric location of the parasite volume in the schizont-iRBC as compared with the trophozoite-iRBC. Yet there still must be an asymmetry in the mass distribution or cell shape, otherwise we would not observe any oscillation in the fluorescence signal (see Fig. 1).

Adhesive dynamics simulations of rolling iRBCs

After having established experimentally that schizonts tend to roll and do not flip as trophozoites do, we next focused on the schizont stage, because it allows us to apply the very efficient modeling framework of adhesive dynamics for spherical cells. This in turn makes it possible to obtain a relatively comprehensive understanding of how molecular determinants and macroscopic rolling behavior are related to each other. To be able to use earlier results for WBCs as a reference case, here we use parameter values that are similar to that case (44,46). As discussed later, the relevant parameter values for iRBCs and WBCs seem to be quite similar.

We first simulated the effect of spatial clustering of receptors into knobs of varying density on the dynamic states of adhesion. Different from earlier work on WBCs, however, we now focus on the effect of knob organization. We used the cluster coefficient ρ from Eq. 4 to vary the degree of clustering. For $N_R = 500$ number of receptors, we chose the three ρ-values 0, 0.4, and 1.0, which result in completely unclustered, intermediate clustered, and completely clustered states, respectively, as shown in Fig. 4, *A*–*C*. The used ligand density of $25/\mu m^2$ corresponds to a typical ligand distance of $d = 200$ nm that is much lower than the typical distance between the receptors (at ~630 nm), so it is not the limiting factor here. In the completely clustered state, there are typically eight receptors in one cluster, similar to the value estimated earlier from experimental data for iRBCs in shear flow (27). In Fig. 4, *D*–*F*, translational and rotational velocities (multiplied by the reference length R) from typical simulation trajectories are shown. Visual inspection shows that as the degree of clustering increases, translation and rotation become increasingly
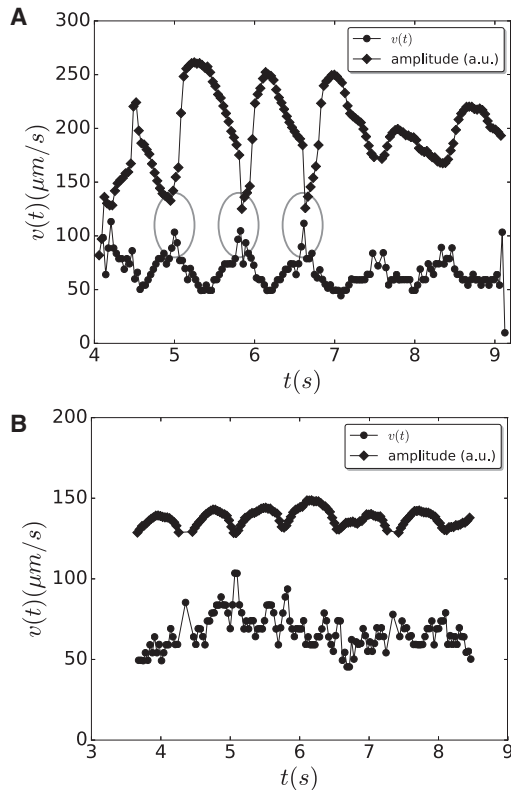
FIGURE 3 Fluorescence amplitude reveals nature of movement in hydrodynamic flow. (*A*) Translational velocity and fluorescence amplitude oscillations are strongly correlated for a trophozoite, indicating flipping motion. (*B*) For a schizont, these correlations are strongly diminished, indicating rolling adhesion of an almost spherical cell. The shear rate is 42 Hz in both cases. Fluorescence movies are provided as Movies S3 and S4.

desynchronized, indicating that rolling adhesion becomes less stable and more irregular as we increase the clustering at the given receptor number. This suggests that increased clustering should be compensated by increased knob density to ensure smooth rolling.

We next measured the state diagram for different degrees of clustering at a constant receptor number. In principle, the state diagram of rolling iRBCs is high-dimensional due to the different model parameters. We first focused on the main molecular determinants of rolling, which are the on- and off-rates. We measured the on-off state diagram from the simulations by varying the dimensionless on-rate ($\pi = \kappa_{\mathrm{on}}/\dot{\gamma}$) and off-rates ($\epsilon = \kappa_{\mathrm{off}}/\dot{\gamma}$), keeping all other parameters fixed. The state diagram captures all the possible dynamic states for the selected range of the dimensionless on- and off-rates. In Fig. 5 A, the on-off state diagram is shown for $N_R = 1000$ unclustered receptors at shear rate $\dot{\gamma} = 100$ Hz. We find very good agreement with earlier results (36,44,46), and in the following we use this state diagram as a reference case. Free motion and transient adhesion-1 are achieved at high off-rates and low on-rates, where the number of bonds become almost negligible, allowing the cell to move freely in shear flow. Rolling adhesion is

achieved at high on-rates and moderate off-rates, which allows for synchronicity between translational and angular movement. Firm adhesion occurs at low off-rates, which inhibits breakage of existing bonds, leading to stoppage of the cell. The intermediate state that occurs between transient adhesion-1 and rolling adhesion or firm adhesion is transient adhesion-2. During transient adhesion-2, the cell frequently adheres for short periods of time (stop-and-go or stick-slip motion).

In Fig. 5 B, the on-off state diagram is shown for a smaller number of receptors than in Fig. 5 A, namely $N_R = 500$, but for different degrees of clustering. We first note that without clustering ($\rho = 0$), the regime of rolling adhesion has somehow decreased, whereas the regime of transient adhesion-2 has expanded, but in general, the state diagram is very similar to the one in Fig. 5 A. If we now increase the clustering coefficient to $\rho = 0.4$ (*solid lines*), the regime of rolling adhesion completely disappears and only transient adhesion exists. Increasing clustering further to $\rho = 1.0$ (*dashed lines*) does not change the state diagram much more. These results suggest that homogeneous coverage of the cell is key for rolling adhesion to occur. Although clustering increases the effective on-rate and decreases the effective off-rate locally, the global effect of reduced encounter for clustered receptors seems to dominate and destabilizes the rolling regime.

As we have seen, homogeneous coverage is required for stable rolling. We now assume such homogenous coverage by knobs and investigate the effect of changing the density of knobs and the number of receptors within each knob. For the latter purpose, we introduce a multiplicity factor *m*. For each knob, we draw the number of receptors from a Poisson distribution with the average *m*. In Fig. 5 C, we show the state diagram for three different knob densities, $N_R = 200$, 500, and 1000, corresponding to knob densities of 1, 2.5, and 10 knobs/μm^2, respectively. Here each knob contains only one receptor ($m = 1$, $N_R = N_k$). There is no rolling adhesion regime for the low density case (*dotted lines*), but it appears at the intermediate density (*solid lines*) and becomes larger for the high density case (*shaded*). The change from low to intermediate densities roughly corresponds to the values at the trophozoite-to-schizont transition.

In Fig. 5 D, we show state diagrams for three different multiplicity factors, $m = 1$, 3, and 5, for $N_R = 200$. Thus the number of receptors is $N_R = 200$, 600, and 1000, but in contrast to (Fig. 5 C), the receptors are now clustered. We see that $N_R = 200$ (*dotted lines*) or 600 (*solid lines*) is not enough to achieve rolling, which only appears for $N_R = 1000$ (*shaded*). Although now the receptors are strongly clustered, their number is sufficiently high to stabilize rolling. In summary, we see that both the knob density and the multiplicity have to be sufficiently high to get stable rolling, and that the threshold lies somewhere between the trophozoite and schizont stages.
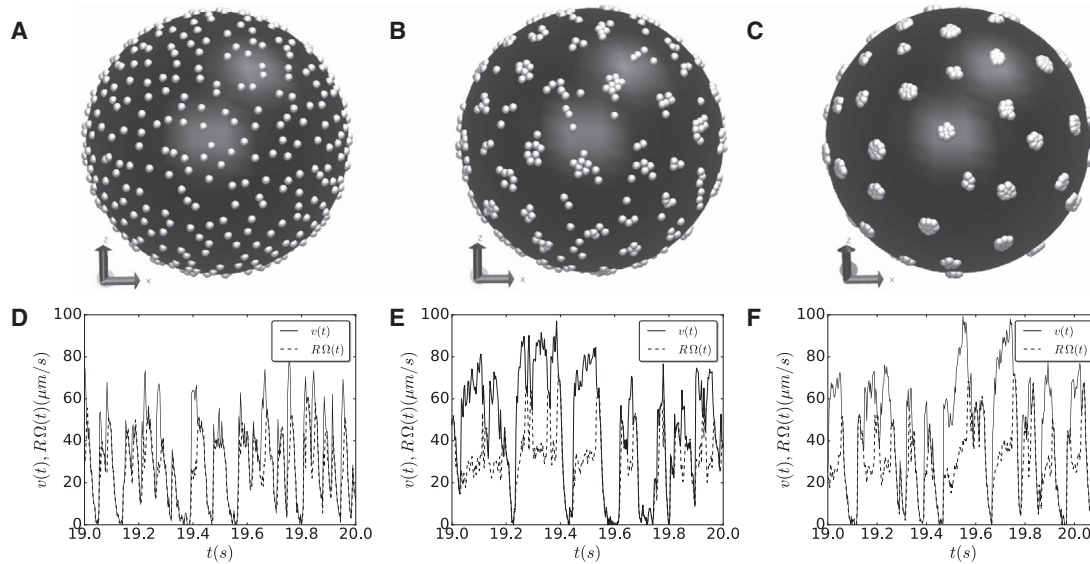
FIGURE 4 Adhesive dynamics simulations of spherical iRBCs—trajectories. Visualization of receptor clustering and translational and rotational velocities of typical trajectories for clustering coefficients $\rho = 0$ (A and D), $\rho = 0.4$ (B and E) and $\rho = 1.0$ (C and F) is given. The total number of receptors in all three cases is $N_R = 500$. Shear rate = 100 Hz, cell radius $R = 4$ μm, spring constant $k = 1$ pN/nm, encounter distance $r_0 = 50$ nm, force scale $F_d = 200$ pN, and ligand density 25/μm^2.

Until now we have discussed the parameters that are controlled by the parasite. We now turn to the external parameters, namely shear rate and ligand density. In all simulation results presented so far, we used a ligand spacing of $d = 200$ nm. For a given knob density, decrease in ligand spacing (corresponding to increase in ligand density) allows the cell to form more bonds, thereby increasing the adhesion and decreasing its velocity, as shown in

Fig. 6 A for $N_R = 1000$. This effect diminishes as the knob density increases to a value comparable to the ligand density. In addition, mean translational and angular velocities (multiplied by R) collapse to the same value for higher knob densities, indicating stable rolling, as revealed in Fig. 6 A by comparing the dashed and solid lines. For high ligand spacing of $d = 200$ nm, both translational and angular velocities collapse to the same value from
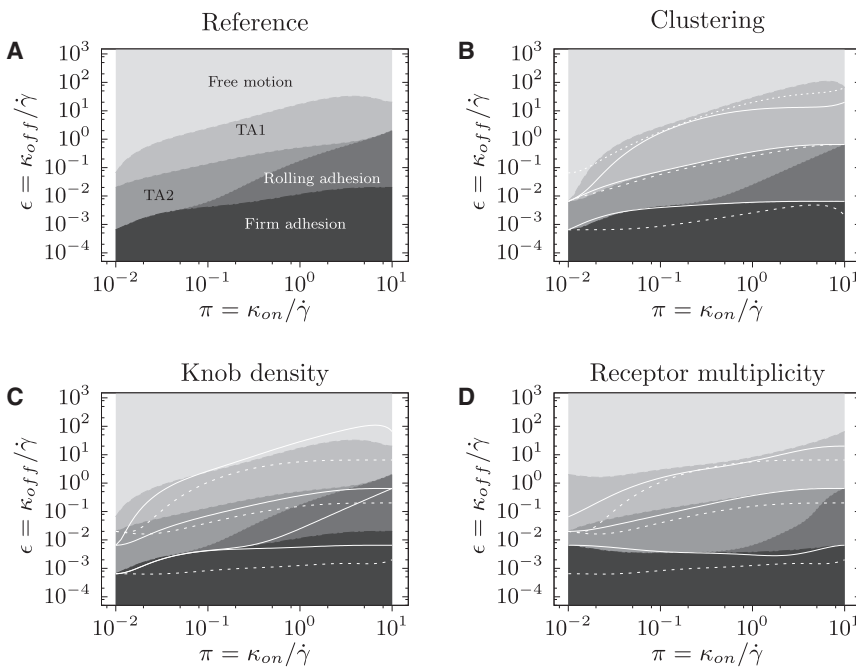

FIGURE 5 Adhesive dynamics simulations of spherical iRBCs—state diagrams. (A) Shown here is on-off state diagram representing different dynamic states for given dimensionless on- and off-rates for $N_R = 1000$. Clustering coefficient $\rho = 0$. (B) Shown here is an on-off state diagram for $N_R = 500$ with different values of clustering coefficients: $\rho = 0$ (shaded), $\rho = 0.4$ (solid lines), and $\rho = 1.0$ (dotted lines). (C) Shown here is on-off state diagram without clustering ($\rho = 0$) for different numbers of one-receptor knobs: $N_R = 200$ (dotted lines), $N_R = 500$ (solid lines), and $N_R = 1000$ (shaded). (D) Shown here is on-off state diagram for $N_R = 200$ and different values of the multiplicity factor: $m = 1$ (dotted lines), $m = 3$ (solid lines), and $m = 5$ (shaded). Model parameters are as in Fig. 4.
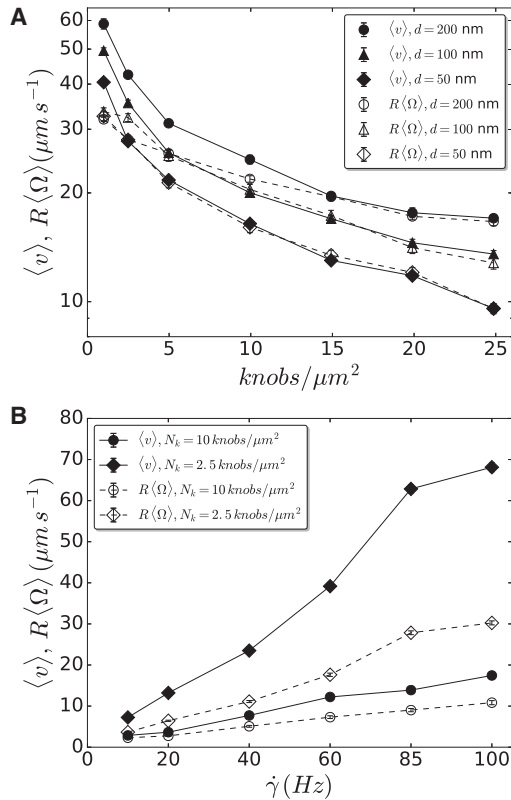
FIGURE 6 Adhesive dynamics simulations of spherical iRBCs—effect of external parameters. (A) A log-linear plot of translational and angular velocities against knob densities is shown for three ligand densities, 50, 100, and 200 nm for $\pi = 2.5$ and $\epsilon = 0.5$. (B) Average translational and angular velocities against shear rate are shown for different knob densities for fixed on-rate $\kappa_{on} = 10$ Hz and fixed off-rate $\kappa_{off} = 5$ Hz.

density 15 knobs/μm^2, whereas for $d = 50$ nm this happens from density 2.5 knobs/μm^2. This means that for low ligand spacing, high knob densities are required to achieve stable rolling, whereas for high ligand spacing, even small knob densities are sufficient to achieve stable rolling. Thus, rolling adhesion of iRBC does not only depend on the structure of the knob system, but also on the adhesive properties of the vascular environment.

In Fig. 6 B, we plot the average translational velocities as a function of shear rate for two different values of the knob densities, which roughly represent the number of knobs present during the trophozoite and schizont stages. Here on- and off-rates are fixed to the absolute values $\kappa_{on} = 10$ Hz and $\kappa_{off} = 5$ Hz. For the range of shear rates investigated, mean translational and angular velocities are found to increase with increasing shear rate, as expected from Bell's equation for the slip bonds modeled here. Note that an increased shear rate also increases the encounter rate, thus potentially decreasing rolling velocity, but this effect seems not to dominate here. We further note that again synchronization between translation and rotation increases with increasing knob density, as discussed above.

Estimating schizont parameters from flow data

In the last section we have aimed at a comprehensive characterization of spherical iRBC rolling using the powerful approach of adhesive dynamics, which, before, has been applied mainly to rolling WBCs. In particular, we have discussed the effect of variations in knob multiplicity and density as well as of bond dynamics while keeping the WBC-case as a reference case. We now turn to a more detailed comparison with schizont stage iRBCs as investigated experimentally. When addressing the comparison with experiments, we first note that all of these determinants are very hard to control in our experiments. For example, the multiplicity of PfEMP-1 receptor multiplicity per knob is still an open experimental issue. Moreover, PfEMP-1 receptors bind to multiple ligands, each with a different bond dynamics. In particular, in our flow chamber experiments both CD36 and ICAM-1 are known to be present, with ICAM-1 being considered to be the main ligand mediating iRBC rolling adhesion. Given this uncertainty in the microscopic parameters, at this stage the main control parameter that allows comparison between experimental and simulated data is the shear rate. We therefore used the effect of shear rate to provide an estimate for the molecular data underlying the observed rolling behavior of schizonts.

We first converted the fluorescence amplitude from Fig. 3 B into an estimate of the angular velocity and found that $R\langle\Omega\rangle/\langle v\rangle \simeq 0.40$, indicating that in our case schizont rolling is not very stable. We speculate that this is related to a relatively low ligand density, as it has been shown earlier that ICAM-1 on HDMECs is present with a surface density of only 6/μm^2 (corresponding to a ligand distance of ~400 nm) (22). As values for the dissociation rate and the internal force scale, we use values of 0.77 Hz and 10 pN, respectively, following literature results for PfEMP-1 binding to CD36 (27). Although the PfEMP1/ICAM-1 pair might have distinct properties, we expect the lifetime and the force scale to be of a similar magnitude. The encounter distance is kept at the established value of $r_0 = 50$ nm from above and the spring constant is reduced slightly to $k = 0.5$ pN/nm to counterbalance the decreased force scale. A similar value has indeed been reported for the PfEMP-1/CSA-bond (71). The knob density is taken to be 10/μm^2 following earlier measurements for the same strain (19). This indicates that both receptor and ligand densities might be limiting. The multiplicity m is taken to be six, according to earlier estimates (27). We vary the association rate and ligand density over a band of reasonable parameters, namely from 100 to 400 nm for the ligand distance (22) and from 0.1 to 10 Hz for the on-rate. Fig. 7 shows that with these values, we get good agreement between our computer simulations and the experimentally measured values, suggesting that we have achieved a reasonable estimate for the molecular parameters of the schizont stage and that the used ranges for ligand distances and on-rates bracket the real values.
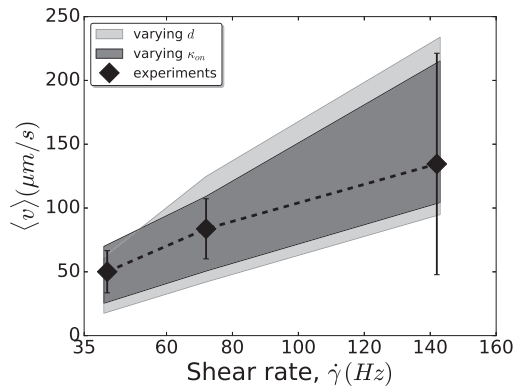
FIGURE 7 Comparison between experimental and simulation results. Experimental data points are provided with standard deviations. Simulation data are shown in two bands: in ligand distance, we cover the range from 100 to 400 nm (*light shaded band*), and in on-rate, the range is from 0.1 to 10 Hz (*dark shaded band*). Off-rate = 0.77 Hz, force scale = 10 pN, and spring constant = 0.5 pN/nm.

We finally investigate the bond dynamics and the adhesive footprint predicted by the adhesive dynamics simulations for the schizonts, a question that in the future could be approached experimentally with fluorescent sensors (56). In Fig. 8, we plot the positions of the knobs on the cell for bond formation (*gray symbols*) and rupture (*colored symbols*). In the second case, the color code reflects the force at which the bond breaks. The full dynamics of bond formation and rupture is shown in Movie S5. We see that new bonds are formed in an effective contact area that is centered around the origin, has a typical radius of ~0.5 μm, and does not depend on shear rate. In contrast, old bonds are ruptured mainly at the rear of the cell, roughly doubling the effective size of the contact area. Although increased shear rate stretches the bond and increases the contact area, this effect is not very large for the values of spring constant and shear rates used here. This agrees with the experimental finding that cell deformation and contact area do not change much at the shear rates used here, both for leukemia cells (56) and for iRBCs (27). The maximal bond extensions in our simulations are 80 and 140 nm for shear rates 42 and 142 Hz, respectively, corresponding to forces of 40 and 70 pN, respectively. This agrees well with rupture forces measured for the PfEMP-1/CSA bond (71). It also corresponds closely to the overall hydrodynamic force resulting from shear flow and, in general, we find that for most of the time, the cell is held at the substrate only by 1–3 bonds.

DISCUSSION

Here we have investigated the adhesive dynamics of schizont stage iRBCs in shear flow at physiological shear rates using both flow chamber experiments on endothelial monolayers and adhesive dynamics computer simulations. Regarding computer simulations, the model is adapted
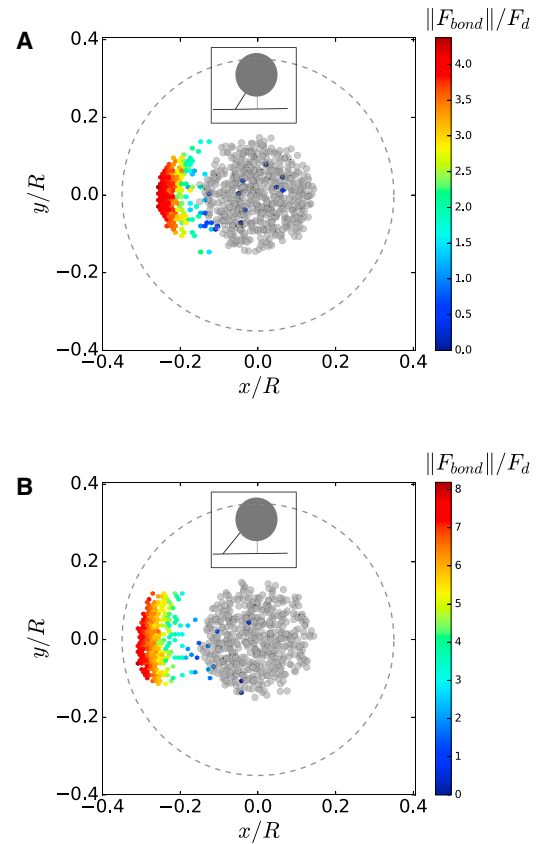

FIGURE 8 Adhesive dynamics simulations of bond dynamics and adhesive footprint. The gray and colored symbols mark the *x*- and *y*-positions of the knobs at which bonds are formed and broken, respectively. The values are shown in the center of mass system of the cell (the *circle* around the origin with radius 0.35 *R* is shown as a guide to the eye). Shear rates are (*A*) 42 Hz and (*B*) 142 Hz. As depicted schematically in the insets, breaking bonds are more stretched at higher shear rates. Full dynamics are shown in Movie S5. To see this figure in color, go online.

from rolling adhesion of WBCs (44), as schizont stage iRBCs share many common features with leukocytes (36). The model cell is assumed to have a spherical shape covered with adhesive knobs containing the PfEMP-1 receptors that mediate adhesion to ligands such as ICAM-1 presented by the vascular endothelium. Our experimental results demonstrate that such an approach is indeed justified in the schizont stage, which is characterized by smooth rolling rather than by the flipping motion observed in the trophozoite stage (Fig. 3). By tracking not only translational, but also rotational velocity (55,56), which in our case can be easily realized by using a fluorescent stain for the parasite, we can compare better with theoretical predictions and conclude that schizont rolling might be just at the onset of stable rolling adhesion. The adhesive dynamics approach is computationally very efficient and allows us to assemble state diagrams representing a complete picture of spherical iRBC rolling adhesion (Fig. 5). To make contacts with our experiments, we have complemented this general approach by an estimate of specific schizont parameters (Fig. 7).

Finally we have predicted the association and dissociation dynamics of the PfEMP-1 bonds and the resulting adhesive footprint (Fig. 8).

As suggested by our model and various experimental observations before, the main determinant of rolling adhesion of iRBCs is the knob density, which increases at least by a factor of two from the trophozoite to the schizont stage. Here we use relatively low numbers for two reasons: first, we experimentally use a malaria strain that is known to have relatively low coverage (19); and second, our computer simulations are expected to overestimate cell stickiness, in particular because it uses a relatively large encounter length and high on-rates to compensate for the fact that a round shape cannot give a flat adhesion region, in contrast to simulations with deformable cells (31,47,48,53). The main uncertainty in our simulations, however, is the unknown multiplicity of receptor localization to the knobs. Although this has been estimated to be ∼7 from flow chamber experiments (27), this estimate is very indirect and a direct measurement has not been achieved yet. In the future, more precise measurements of receptor multiplicity have to be made to achieve a more detailed understanding of the main determinants of iRBC-rolling. We note that by measuring comprehensive state diagrams as a function of all model parameters, our systematic approach is well suited to adopt new experimental results as they will become available in the future.

Similar remarks as for the knob structure are in order also for the ligand structure on the substrate. In our simulations we have distributed the ligands on a substrate with variable but homogeneous ligand density. In the experiments, however, they are presented on top of an endothelial monolayer that is bound to be rough and heterogeneous, and for which the exact spatial distribution is not known. Although this approach is of high physiological relevance and, for example, would allow us to study such effects as inflammation of the endothelium in response to a malaria infection, for future quantitative studies it might also be very instructive to use more defined model systems, such as supported lipid bilayers, for which ligand density and ligand clustering can be tuned in a systematic manner (19).

As common in adhesive dynamics simulations (38,39, 44,46), the complex mechanical response of the PfEMP-1 bond, which here is assumed to be mainly formed to ICAM-1, is lumped into one effective spring constant k. Here we use a value of 0.5 pN/nm, which falls into the generic range of spring constants used for adhesive dynamics simulations (38) and modeling adhesion contacts (72). It is also similar to values reported from single molecule experiments for actin-myosin crossbridges (73) and for the PfEMP-1/CSA bond (71). Earlier work on adhesion contacts formed by adhering vesicles suggests that the effective spring constant is a complex convolution of membrane and bond contributions (72). If it was possible to experimentally measure the mean squared fluctuation amplitude σ of the membrane, than the effective spring constant would follow as $k = k_{B}T/\sigma$. For a membrane with bending stiffness κ and harmonic confinement parameter γ, one can calculate the corresponding spring constant as $k_m = 8\sqrt{\kappa\gamma}$ (72,74). Using typical values $\kappa = 10\ k_{B}T$ and $\gamma = 10^8\ J/m^4$, we get $k_m = 0.02$ pN/nm (corresponding to a fluctuation amplitude of 15 nm), suggesting that membrane deformations might dominate because mechanically they provide the softer spring. However, exactly at the position of the bond, one finds $\sigma = k_{B}T/(k_m + k)$, thus the bond spring constant k dominates over the membrane spring constant k_m in such a statistical treatment (72). Moreover, we expect that a more detailed analysis would also give anharmonic contributions, as recently demonstrated for vesicle adhesion (75).

In our context, the spring constant does not only have to represent the typical deformation of the adhesive bond, leading to the formation of an effective contact area, but also the force leading to dissociation of the receptor-ligand bond according to the Bell's equation. Both aspects seem to be captured well in our work, because the bond dynamics leads to good agreement with experiments (Fig. 7) and because the resulting contact area is of the same order of magnitude as the experimentally measured ones (Fig. 8) (27,56), despite the fact that we do not model deformable cells, for which similar contact areas have been found in simulations (47). However, we also note that the peak force of 70 pN reported in our adhesive dynamics simulations already comes close to the range 150–250 pN, which has been reported for unfolding of immunoglobulin domains as they are also present in the PfEMP-1 binding partners ICAM-1 and CD36 (76). The spring constant of the immunoglobulin IgG1 has been measured to be 10.9 pN/nm (77) and the peak force simulated here would lead to a deformation of 6.4 nm, which in practice could not be provided by the molecular structure, thus unfolding had to result. However, the mechanics of PfEMP-1 bonds are certainly more complex than suggested by considering only one effective spring constant, and as explained above, we expect that the effective deformation will also be determined by membrane and cytoskeletal mechanics and fluctuations, in particular by the spectrin network of the iRBC. We expect that more detailed experimental results will become available in the future and then can be incorporated into adhesive dynamics simulations.

As we have observed experimentally, motion in the trophozoite stage seems to resemble flipping rather than rolling, as predicted earlier by computer simulations (31,53,54). To address this important issue, one requires computer models for deformable cells. Although the stiffness of the cell envelope has been measured and modeled as a function of developmental stage (29,31), it is not clear if the commonly used assumption of a homogeneous membrane is entirely justified. In the ring and trophozoite stages, the parasite is known to stay close to its site of invasion, and this could result in a heterogeneous knob structure. Even if

Dasanna et al.

the mechanical properties of the cell envelope might appear to be homogeneous in cell stretching experiments, in practice there might be local variations in knob structure and mechanics that matter for rolling adhesion. Like the issues of knob density, receptor multiplicity, and ligand presentation, elucidating this important aspect of the blood stage of a malaria infection also requires a combination of computational and experimental approaches, such that in the future we can finally achieve a quantitative and comprehensive understanding of the biophysics of iRBC in shear flow.

SUPPORTING MATERIAL

Five movies are available at http://www.biophysj.org/biophysj/supplemental/
S0006-3495(17)30386-7.

AUTHOR CONTRIBUTIONS

U.S.S. and M.L. conceived the research. A.K.D. performed the computer simulations. C.L. performed the experiments. A.K.D. and U.S.S. wrote the manuscript. All authors analyzed the data and revised the manuscript.

ACKNOWLEDGMENTS

REFERENCES

1. Miller, L. H., D. I. Baruch, …, O. K. Doumbo. 2002. The pathogenic basis of malaria. *Nature*. 415:673–679.

2. Storm, J., and A. G. Craig. 2014. Pathogenesis of cerebral malaria—inflammation and cytoadherence. *Front. Cell. Infect. Microbiol.* 4:100.

3. Bannister, L. H., J. M. Hopkins, …, G. H. Mitchell. 2000. A brief illustrated guide to the ultrastructure of *Plasmodium falciparum* asexual blood stages. *Parasitol. Today.* 16:427–433.

4. Maier, A. G., B. M. Cooke, …, L. Tilley. 2009. Malaria parasite proteins that remodel the host erythrocyte. *Nat. Rev. Microbiol.* 7:341–354.

5. Cyrklaff, M., C. P. Sanchez, …, M. Lanzer. 2011. Hemoglobins S and C interfere with actin remodeling in *Plasmodium falciparum*-infected erythrocytes. *Science.* 334:1283–1286.

6. Cyrklaff, M., C. P. Sanchez, …, M. Lanzer. 2012. Host actin remodeling and protection from malaria by hemoglobinopathies. *Trends Parasitol.* 28:479–485.

7. Kilian, N., S. Srismith, …, M. Lanzer. 2015. Hemoglobin S and C affect protein export in *Plasmodium falciparum*-infected erythrocytes. *Biol. Open.* 4:400–410.

8. Lew, V. L., T. Tiffert, and H. Ginsburg. 2003. Excess hemoglobin digestion and the osmotic stability of *Plasmodium falciparum*-infected red blood cells. *Blood.* 101:4189–4194.

9. Mauritz, J. M. A., A. Esposito, …, V. L. Lew. 2009. The homeostasis of *Plasmodium falciparum*-infected red blood cells. *PLoS Comput. Biol.* 5:e1000339.

10. Esposito, A., J.-B. Choimet, …, T. Tiffert. 2010. Quantitative imaging of human red blood cells infected with *Plasmodium falciparum*. *Biophys. J.* 99:953–960.

11. Waldecker, M., A. K. Dasanna, …, M. Lanzer. 2016. Differential time-dependent volumetric and surface area changes and delayed induction of new permeation pathways in haemoglobinopathic erythrocytes. *Cell. Microbiol.* 19:e12650.

12. Abkarian, M., G. Massiera, …, C. Braun-Breton. 2011. A novel mechanism for egress of malarial parasites from red blood cells. *Blood.* 117:4118–4124.

13. Callan-Jones, A., O. E. Albarran Arriagada, …, M. Abkarian. 2012. Red blood cell membrane dynamics during malaria parasite egress. *Biophys. J.* 103:2475–2483.

14. Aikawa, M., J. R. Rabbege, …, L. H. Miller. 1983. Electron microscopy of knobs in *Plasmodium falciparum*-infected erythrocytes. *J. Parasitol.* 69:435–437.

15. Gruenberg, J., D. R. Allred, and I. W. Sherman. 1983. Scanning electron microscope-analysis of the protrusions (knobs) present on the surface of *Plasmodium falciparum*-infected erythrocytes. *J. Cell Biol.* 97:795–802.

16. Allred, D. R., J. E. Gruenberg, and I. W. Sherman. 1986. Dynamic rearrangements of erythrocyte membrane internal architecture induced by infection with *Plasmodium falciparum*. *J. Cell Sci.* 81:1–16.

17. Nagao, E., O. Kaneko, and J. A. Dvorak. 2000. *Plasmodium falciparum*-infected erythrocytes: qualitative and quantitative analyses of parasite-induced knobs by atomic force microscopy. *J. Struct. Biol.* 130:34–44.

18. Quadt, K. A., L. Barfod, …, L. Hviid. 2012. The density of knobs on *Plasmodium falciparum*-infected erythrocytes depends on developmental age and varies among isolates. *PLoS One.* 7:e45658.

19. Rieger, H., H. Y. Yoshikawa, …, M. Lanzer. 2015. Cytoadhesion of *Plasmodium falciparum*-infected erythrocytes to chondroitin-4-sulfate is cooperative and shear enhanced. *Blood.* 125:383–391.

20. Turner, G. D., H. Morrison, …, B. Nagachinta. 1994. An immunohistochemical study of the pathology of fatal malaria. Evidence for widespread endothelial activation and a potential role for intercellular adhesion molecule-1 in cerebral sequestration. *Am. J. Pathol.* 145:1057–1069.

21. Newbold, C., P. Warn, …, K. Marsh. 1997. Receptor-specific adhesion and clinical disease in *Plasmodium falciparum*. *Am. J. Trop. Med. Hyg.* 57:389–398.

22. McCormick, C. J., A. Craig, …, A. R. Berendt. 1997. Intercellular adhesion molecule-1 and CD36 synergize to mediate adherence of *Plasmodium falciparum*-infected erythrocytes to cultured human microvascular endothelial cells. *J. Clin. Invest.* 100:2521–2529.

23. Yipp, B. G., S. Anand, …, M. Ho. 2000. Synergism of multiple adhesion molecules in mediating cytoadherence of *Plasmodium falciparum*-infected erythrocytes to microvascular endothelial cells under flow. *Blood.* 96:2292–2298.

24. Herricks, T., M. Avril, …, P. K. Rathod. 2013. Clonal variants of *Plasmodium falciparum* exhibit a narrow range of rolling velocities to host receptor CD36 under dynamic flow conditions. *Eukaryot. Cell.* 12:1490–1498.

25. Shi, H., Z. Liu, …, C. T. Lim. 2013. Life cycle-dependent cytoskeletal modifications in *Plasmodium falciparum* infected erythrocytes. *PLoS One.* 8:e61170.

26. Zhang, Y., C. Huang, …, S. Suresh. 2015. Multiple stiffening effects of nanoscale knobs on human red blood cells infected with *Plasmodium falciparum* malaria parasite. *Proc. Natl. Acad. Sci. USA.* 112:6068–6073.

27. Xu, X., A. K. Efremov, …, J. Cao. 2013. Probing the cytoadherence of malaria infected red blood cells under flow. *PLoS One.* 8:e64763.

28. Cranston, H. A., C. W. Boylan, …, D. J. Krogstad. 1984. *Plasmodium falciparum* maturation abolishes physiologic red cell deformability. *Science.* 223:400–403.

29. Suresh, S., J. Spatz, …, T. Seufferlein. 2005. Connections between single-cell biomechanics and human disease states: gastrointestinal cancer and malaria. *Acta Biomater.* 1:15–30.

30. Park, Y., M. Diez-Silva, …, S. Suresh. 2008. Refractive index maps and membrane dynamics of human red blood cells parasitized by *Plasmodium falciparum*. *Proc. Natl. Acad. Sci. USA.* 105:13730–13735.

31. Fedosov, D. A., B. Caswell, …, G. E. Karniadakis. 2011. Quantifying the biophysical characteristics of *Plasmodium falciparum*-parasitized red blood cells in microcirculation. *Proc. Natl. Acad. Sci. USA.* 108:35–39.

32. Fedosov, D. A., H. Lei, …, G. E. Karniadakis. 2011. Multiscale modeling of red blood cell mechanics and blood flow in malaria. *PLoS Comput. Biol.* 7:e1002270.

33. Ye, T., N. Phan-Thien, …, C. T. Lim. 2013. Stretching and relaxation of malaria-infected red blood cells. *Biophys. J.* 105:1103–1109.

34. Springer, T. A. 1994. Traffic signals for lymphocyte recirculation and leukocyte emigration: the multistep paradigm. *Cell.* 76:301–314.

35. McEver, R. P., and C. Zhu. 2010. Rolling cell adhesion. *Annu. Rev. Cell Dev. Biol.* 26:363–396.

36. Helms, G., A. K. Dasanna, …, M. Lanzer. 2016. Modeling cytoadhesion of *Plasmodium falciparum*-infected erythrocytes and leukocytes-common principles and distinctive features. *FEBS Lett.* 590:1955–1971.

37. Cooke, B. M., A. R. Berendt, …, G. B. Nash. 1994. Rolling and stationary cytoadhesion of red blood cells parasitized by *Plasmodium falciparum*: separate roles for ICAM-1, CD36 and thrombospondin. *Br. J. Haematol.* 87:162–170.

38. Hammer, D. A., and S. M. Apte. 1992. Simulation of cell rolling and adhesion on surfaces in shear flow: general results and analysis of selectin-mediated neutrophil adhesion. *Biophys. J.* 63:35–57.

39. Hammer, D. A. 2014. Adhesive dynamics. *J. Biomech. Eng.* 136:021006.

40. Bhatia, S. K., M. R. King, and D. A. Hammer. 2003. The state diagram for cell adhesion mediated by two receptors. *Biophys. J.* 84:2671–2690.

41. Caputo, K. E., D. Lee, …, D. A. Hammer. 2007. Adhesive dynamics simulations of the shear threshold effect for leukocytes. *Biophys. J.* 92:787–797.

42. Korn, C., and U. S. Schwarz. 2006. Efficiency of initiating cell adhesion in hydrodynamic flow. *Phys. Rev. Lett.* 97:138103.

43. Korn, C. B., and U. S. Schwarz. 2007. Mean first passage times for bond formation for a Brownian particle in linear shear flow above a wall. *J. Chem. Phys.* 126:095103.

44. Korn, C. B., and U. S. Schwarz. 2008. Dynamic states of cells adhering in shear flow: from slipping to rolling. *Phys. Rev. E Stat. Nonlin. Soft Matter Phys.* 77:041904.

45. Bose, S., S. K. Das, …, R. Karnik. 2010. A semianalytical model to study the effect of cortical tension on cell rolling. *Biophys. J.* 99:3870–3879.

46. Ramesh, K. V., R. Thaokar, …, R. Prabhakar. 2015. Significance of thermal fluctuations and hydrodynamic interactions in receptor-ligand-mediated adhesive dynamics of a spherical particle in wall-bound shear flow. *Phys. Rev. E Stat. Nonlin. Soft Matter Phys.* 91:022302.

47. Jadhav, S., C. D. Eggleton, and K. Konstantopoulos. 2005. A 3-D computational model predicts that cell deformation affects selectin-mediated leukocyte rolling. *Biophys. J.* 88:96–104.

48. Luo, Z. Y., and B. F. Bai. 2016. State diagram for adhesion dynamics of deformable capsules under shear flow. *Soft Matter.* 12:6918–6925.

49. Sun, C., C. Migliorini, and L. L. Munn. 2003. Red blood cells initiate leukocyte rolling in postcapillary expansions: a lattice Boltzmann analysis. *Biophys. J.* 85:208–222.

50. Noguchi, H., and G. Gompper. 2005. Shape transitions of fluid vesicles and red blood cells in capillary flows. *Proc. Natl. Acad. Sci. USA.* 102:14159–14164.

51. Pivkin, I. V., and G. E. Karniadakis. 2008. Accurate coarse-grained modeling of red blood cells. *Phys. Rev. Lett.* 101:118105.

52. Fedosov, D. A., B. Caswell, and G. E. Karniadakis. 2010. A multiscale red blood cell model with accurate mechanics, rheology, and dynamics. *Biophys. J.* 98:2215–2225.

53. Fedosov, D. A., B. Caswell, and G. E. Karniadakis. 2011. Wall shear stress-based model for adhesive dynamics of red blood cells in malaria. *Biophys. J.* 100:2084–2093.

54. Fedosov, D. A. 2010. Multiscale modeling of blood flow and soft matter. Ph.D. thesis. Brown University, Providence, RI.

55. Suo, J., E. E. Edwards, …, S. N. Thomas. 2016. Force and torque on spherical particles in micro-channel flows using computational fluid dynamics. *R. Soc. Open Sci.* 3:160298.

56. Li, I. T., T. Ha, and Y. R. Chemla. 2017. Mapping cell surface adhesion by rotation tracking and adhesion footprinting. *Sci. Rep.* 7:44502.

57. Trager, W., and J. B. Jensen. 1976. Human malaria parasites in continuous culture. *Science.* 193:673–675.

58. Lambros, C., and J. P. Vanderberg. 1979. Synchronization of *Plasmodium falciparum* erythrocytic stages in culture. *J. Parasitol.* 65:418–420.

59. Goodyer, I. D., J. Johnson, …, D. J. Hayes. 1994. Purification of mature-stage *Plasmodium falciparum* by gelatine flotation. *Ann. Trop. Med. Parasitol.* 88:209–211.

60. Claessens, A., and J. A. Rowe. 2012. Selection of *Plasmodium falciparum* parasites for cytoadhesion to human brain endothelial cells. *J. Vis. Exp.* 59:e3122.

61. Uhlemann, A.-C., T. Staalsoe, …, L. Hviid. 2000. Analysis of *Plasmodium falciparum*-infected red blood cells. *MACS & more.* 4:7–8.

62. Ermak, D. L., and J. A. McCammon. 1978. Brownian dynamics with hydrodynamic interactions. *J. Chem. Phys.* 69:1352.

63. Bell, G. I. 1981. Estimate of the sticking probability for cells in uniform shear flow with adhesion caused by specific bonds. *Cell Biophys.* 3:289–304.

64. Marshall, B. T., M. Long, …, C. Zhu. 2003. Direct observation of catch bonds involving cell-adhesion molecules. *Nature.* 423:190–193.

65. Destainville, N. 2008. Cluster phases of membrane proteins. *Phys. Rev. E Stat. Nonlin. Soft Matter Phys.* 77:011905.

66. Mani, E., W. Lechner, …, P. G. Bolhuis. 2014. Equilibrium and non-equilibrium cluster phases in colloids with competing interactions. *Soft Matter.* 10:4479–4486.

67. Goldman, A. J., R. G. Cox, and H. Brenner. 1967. Slow viscous motion of a sphere parallel to a plane wall—I. Motion through a quiescent fluid. *Chem. Eng. Sci.* 22:637–651.

68. Chien, S. 1971. Present state of blood rheology. Hemodilution, theoretical basis and clinical application. *In* Proceedings of the International Symposium, Rotach-Egern. K. Messmer and H. Schonbein, editors. Karger, Basel, Switzerland.

69. Lipowsky, H. H. 1985. Shear stress in the circulation. *In* Flow-Dependent Regulation of Vascular Function. Oxford University Press, Oxford, UK, pp. 28–45.

70. Lipowsky, H. H. 2005. Microvascular rheology and hemodynamics. *Microcirculation.* 12:5–15.

71. Carvalho, P. A., M. Diez-Silva, …, S. Suresh. 2013. Cytoadherence of erythrocytes invaded by *Plasmodium falciparum*: quantitative contact-probing of a human malaria receptor. *Acta Biomater.* 9:6349–6359.

72. Bihr, T., U. Seifert, and A.-S. Smith. 2012. Nucleation of ligand-receptor domains in membrane adhesion. *Phys. Rev. Lett.* 109:258101.

73. Veigel, C., M. L. Bartoo, …, J. E. Molloy. 1998. The stiffness of rabbit skeletal actomyosin cross-bridges determined with an optical tweezers transducer. *Biophys. J.* 75:1424–1438.

74. Gov, N. S., and S. A. Safran. 2005. Red blood cell membrane fluctuations and shape controlled by ATP-induced cytoskeletal defects. *Biophys. J.* 88:1859–1874.

75. Schmidt, D., C. Monzel, …, A.-S. Smith. 2014. Signature of a nonharmonic potential as revealed from a consistent shape and fluctuation analysis of an adherent membrane. *Phys. Rev. X.* 4:021023.

76. Bullard, B., T. Garcia, …, A. F. Oberhauser. 2006. The molecular elasticity of the insect flight muscle proteins projectin and kettin. *Proc. Natl. Acad. Sci. USA.* 103:4451–4456.

77. Stingaciu, L. R., O. Ivanova, …, D. Richter. 2016. Fast antibody fragment motion: flexible linkers act as entropic spring. *Sci. Rep.* 6:22148.